

## Supplementary information

### Inconsistency between superstructure stability and long-term cyclability of oxygen redox in Na layered oxides

Hui Liu,<sup>‡,a</sup> Chong Zhao,<sup>‡,a</sup> Xiang Wu,<sup>a</sup> Chunjing Hu,<sup>a</sup> Fushan Geng,<sup>a</sup> Ming Shen,<sup>a</sup> Bei Hu,<sup>b</sup> Bingwen Hu,<sup>a</sup> and Chao Li<sup>\*a</sup>

<sup>a</sup>Shanghai Key Laboratory of Magnetic Resonance, School of Physics and Electronic Science, East China Normal University, Shanghai 200241, P. R. China

<sup>b</sup>National Key Laboratory of Science and Technology on Micro/Nano Fabrication, Key Laboratory for Thin Film and Microfabrication of the Ministry of Education, Department of Micro/Nano Electronics, School of Electronic Information and Electrical Engineering, Shanghai Jiao Tong University, Shanghai 200240, P. R. China

<sup>‡</sup>These two authors contributed equally to this work.

\*E-mail: lchao@phy.ecnu.edu.cn

**Supplementary Note 1.** When tested within the voltage range of 3.5-4.7 V (vs. Na<sup>+</sup>/Na), the initial discharge capacities of P2-NLMO-r and P3-NLMO-r are 73.0 and 73.6 mAh g<sup>-1</sup>, respectively (**Figure S9-S10**), showing a similar oxygen anionic redox (OAR) activity during the initial cycling (0.25 mol Na<sup>+</sup> ions). However, the P2-NLMO-r cathode only maintains 29.4 mAh g<sup>-1</sup> after ten cycles while P3-NLMO-r maintains 59.4 mAh g<sup>-1</sup> (nearly twice that of P2-NLMO-r). The reversible capacity continually declines for P2-NLMO-r and nearly zero mAh g<sup>-1</sup> can be delivered after 100 cycles, while the P3-NLMO-r cathode still maintains a reversible capacity of 30.5 mAh g<sup>-1</sup>. Besides, the Coulombic efficiency of P2-NLMO-r maintains at a lower level and frequently vibrates during the whole 100 cycles while the P3-NLMO-r maintains at around 97%. The polarization between charge and discharge also increase dramatically for P2-NLMO-r over cycling while the polarization is much smaller for P3-NLMO-r,<sup>1</sup> further demonstrating the poorer Na<sup>+</sup> insertion/extraction kinetics in P2-NLMO-r when only OAR occurs. On the other hand, the average voltage of discharge (AVoD) for P2-NLMO-r suffers from a dramatic decay during the initial ten cycles and then remains relatively stable until 100 cycles. Comparatively, the AVoD of P3-NLMO-r is stable during the whole 100 cycles. Taken together, P2-NLMO-r shows much worse cycling stability than that of P3-NLMO-r within the voltage range of 3.5-4.7 V, demonstrating its poor OAR reversibility when Mn redox does not occur. The above result is also consistent with a previous report by Gu and Hu et al.<sup>2</sup>

**Supplementary Note 2.** In order to investigate the structural transformation at long-range scale, operando XRD studies were performed, as presented in **Figure S11-S12**. On charging, the diffraction peaks belonging to the P2 phase gradually decline in intensity, implying the transition from P2-type layer stacking to O2-type with reduced interlayer spacing (**Figure S11**). However, no evident peaks belonging to the O2 phase (the characteristic (002) and (101) peaks are located at  $16.5^\circ$  and  $37^\circ$  in  $2\theta$ , respectively) were detected, which means that the O2-type phase at charged state is not well crystallized. In this regard, Sung et al. have proved the coexistence of Z-phase (that is, a continuously changing intergrowth structure which evolves from P2 to O2 through the OP4 structure as an intermediate<sup>3</sup>) and original P2-phase upon desodiation by operando synchrotron XRD analysis,<sup>4</sup> which coincides well with our results here. Besides, the crystalline P2-phase can progressively recover during the subsequent discharging, manifesting a highly reversible structural evolution.

Although the peak intensities of P3-NLMO-r in the operando XRD device are relatively poor compared to the P2-NLMO-r series, a gradual transition from P3-type layer stacking to O3-type can also be determined by the gradual decay in intensity for the characteristic (003) and (006) peaks (**Figure S12**). This is consistent with the formation of P'3 phase as reported by Hu's group and Kang's group.<sup>2, 5</sup> Likewise, the crystalline P3-phase can gradually regain upon discharging, demonstrating a reversible crystal structure evolution.

**Supplementary Note 3.** The evolution of Li local environment in P2- and P3-NLMO-r upon Na<sup>+</sup> (de)intercalation was inspected via <sup>7</sup>Li pj-MATPASS (pj = projection, MAT: magic-angle turning, PASS: phase-adjusted sideband separation) NMR. For pristine P2- and P3-NLMO-r (**Figure S16-S17**), the dominant resonances at around 2000 ppm belong to Li sites in the TM layer (Li<sub>TM</sub>), and the splitting into two resonances for P2-NLMO-r probably originates from the surface chemical reaction when contacting the electrolyte (catalytic effect). In addition, the minor resonance at around 700 ppm is rationally assigned to Li sites in the AM layer (Li<sub>AM</sub>).<sup>6, 7</sup> Since Li is improbable to occupy the prismatically coordinated Na sites, Li<sub>AM</sub> in pristine P2- and P3-NLMO-r should exist in the minute amount of O-type stacking faults, the formation of which is hard to avoid during high-temperature solid-state reaction.

On charging, both P2-NLMO-r and P3-NLMO-r show significant migration of Li<sup>+</sup> from the TM layer into octahedrally coordinated sites in the AM layer, suggesting the progressive conversion of P-type layers into O-type to accommodate the Li<sup>+</sup> ions.<sup>8, 9</sup> Such out-of-plane Li<sup>+</sup> displacement is not completely accomplished since a reasonable amount of Li<sub>TM</sub> still maintains at the full-charged (FC) state. The difference is that the Li<sub>AM</sub> in charged P2-NLMO-r exists in O2-type domain while the Li<sub>AM</sub> in charged P3-NLMO-r exists in O3-type domain. Of note, a wider distribution of Li<sub>AM</sub> peaks is seen for P3-NLMO-r at the full-charged state as compared to that of P2-NLMO-r (as seen more clearly in **Figure S18**), which could be associated with its higher amount of Na<sup>+</sup> in the O-type domain that leads to the well-ordered abruption of different Li environments. On discharging, the migrated Li<sup>+</sup> ions can unremittingly reoccupy the

sites in the TM layer and a nearly 100% Li<sub>TM</sub> signal recovery is observed at the full-discharged (FD) state for both P2-NLMO-r and P3-NLMO-r, suggesting the presence of Li again dominantly in their original octahedral sites in TM layer. Moreover, the local structural evolution of Li<sup>+</sup> during the second charging is nearly the repetition of the initial charging, furthering elucidating the reversibility of Li<sup>+</sup> displacement process for both P2- and P3-NLMO-r.

To directly see the Li distribution during the first charge/discharge and second charge processes, integration of the Li signals for both materials have also been plotted and shown in the histograms in **Figure 2a, b**. The proportion of Li<sub>AM</sub> for desodiated P2-NLMO-r is higher than that of desodiated P3-NLMO-r during the whole charge/discharge process, implying the higher amount of Li<sup>+</sup> in O-type domains during OAR process. Such difference in the proportion of Li<sub>AM</sub> on charging also exists in the 10th and 20th cycle (**Figure S19**), persuasively confirming the more prominent out-of-plane Li<sup>+</sup> displacement in P2-NLMO-r during repeated OAR process. However, such Li<sup>+</sup> displacement is reversible upon discharging for both P2- and P3-NLMO-r, which maintains the characteristic Na—O—Li configurations.

**Supplementary Note 4.** In principle,  $^{23}\text{Na}$  with  $I = 3/2$  is a quadrupolar nucleus and owns a large second-order quadrupolar interaction, engendering a field-dependent quadrupolar induced shift ( $\delta_{\text{QIS}}$ ) in addition to field-independent  $\delta_{\text{iso}}$ . Upon cooling, the position of the isotropic  $^{23}\text{Na}$  signals drift leftward (**Figure S21-S22**); that is, the magnetic susceptibility increases as the temperature decreases, which reflects its paramagnetic nature and the  $^{23}\text{Na}$  shift is mainly governed by the Fermi contact interaction.<sup>10</sup> In other words, the contribution from field-dependent  $\delta_{\text{QIS}}$  is relatively small for P2- and P3-NLMO-r. For both P2- and P3-NLMO-r, a continuous broadening of the peaks occurs upon cooling because Na hopping among sites becomes much slower than the line width of the NMR peak (in kHz).<sup>11</sup> Notably, the full-charged (FC) and 3.85 V-discharged P2-NLMO-r exhibit more rapid  $^{23}\text{Na}$  signal broadening during the cooling process compared to P3-NLMO-r, suggesting a smaller rate of  $\text{Na}^+$  hopping. Note that this result was achieved with a higher number of scans (200000 *versus* 100000). The rapid  $\text{Na}^+$  hopping in P3-NLMO-r might further contribute to the reconstruction of superstructure ordering upon discharge, which corresponds well with the ex situ  $^{23}\text{Na}/^7\text{Li}$  solid-state NMR and high-energy XRD results.

**Supplementary Note 5.** Notably, a 6-fold hyperfine splitting feature of EPR is captured at the deeply charged states of P2- and P3-NLMO-r especially during the second and third cycling process (**Figure 3** and **Figure S23**), as can be seen more clearly in **Figure S24**. Such feature implies that the electron dipole–dipole coupling between Mn<sup>4+</sup>/O<sup>·-</sup> is anisotropic at these desodiated states.<sup>12, 13</sup> It has been proved by <sup>7</sup>Li pj-MATPASS NMR that both P2- and P3-NLMO-r show progressive migration of Li<sup>+</sup> from the TM layer into octahedrally coordinated sites in the AM layer upon charging, resulting in the formation of vacancies in the TM layer. Hence, we tentatively attribute the characteristic 6-fold hyperfine splitting feature to the pronounced vacancy shrinkage at the deeply charged state, the formation of which has also been observed via operando EPR in OAR-active Na<sub>2</sub>Mn<sub>3</sub>O<sub>7</sub> (or Na<sub>4/7</sub>[□<sub>1/7</sub>Mn<sub>6/7</sub>]O<sub>2</sub> where □ = native Mn vacancies).<sup>14</sup> Of note, such 6-fold hyperfine splitting feature was not observed via ex situ EPR measurements (**Figure S25**), suggesting that the "vacancy shrinking" structure is a thermodynamically metastable state.

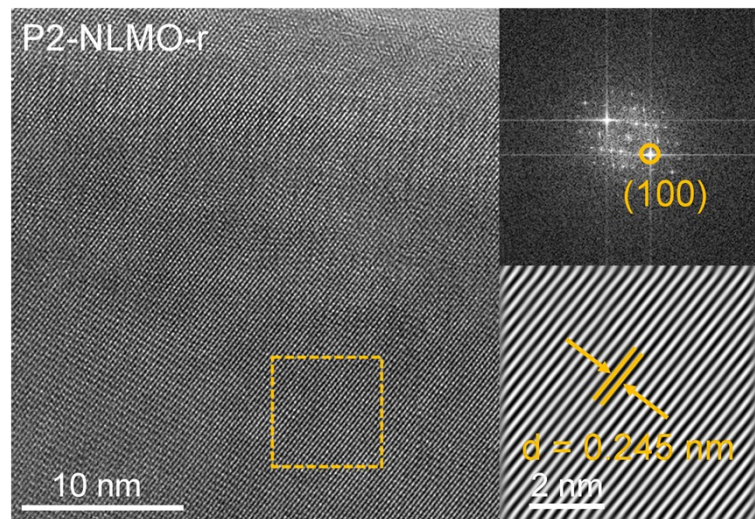


**Figure S1.** HRTEM images and the corresponding Fourier transform (FT) and inversed Fourier transform (IFT) patterns of P2-NLMO-r. The lattice fringes with 0.245 nm within P2-NLMO-r is recognized as the (100) plane of the P2 structure.

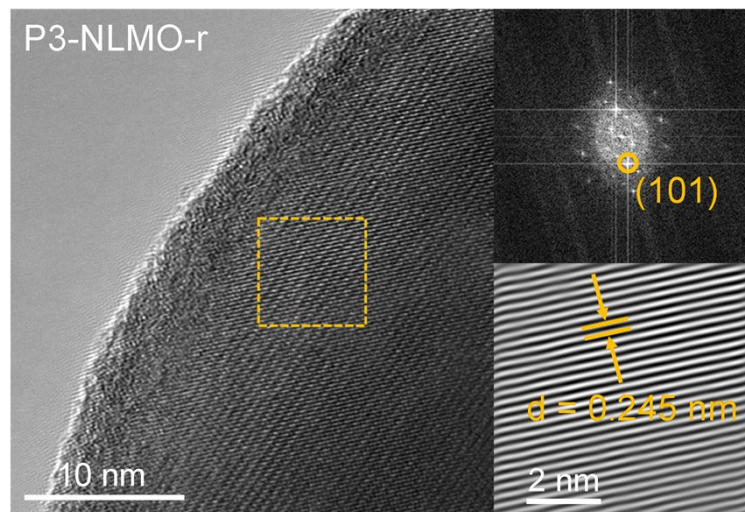


**Figure S2.** HRTEM images and the corresponding Fourier transform (FT) and inversed Fourier transform (IFT) patterns of P3-NLMO-r. The lattice fringes with 0.245 nm within P3-NLMO-r is recognized as the (101) plane of the P3 structure.

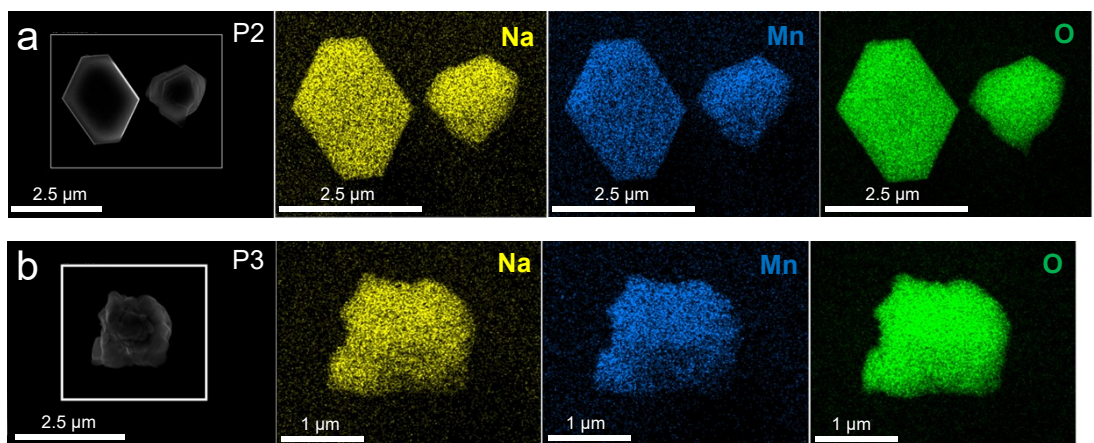


**Figure S3.** SEM and the corresponding EDS mapping images of (a) P2-NLMO-r and (b) P3-NLMO-r compounds. Obviously, Na, Mn, and O elements are evenly distributed in the P2- and P3-NLMO-r particles.

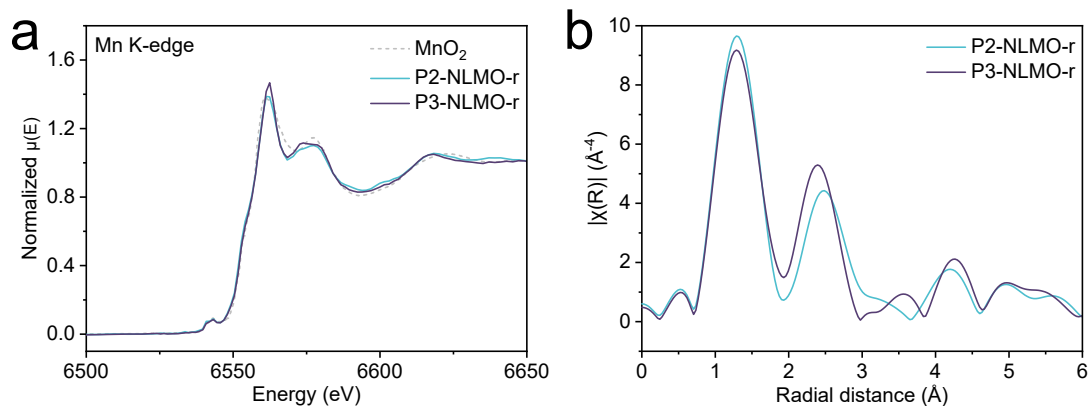


**Figure S4.** (a) Normalized Mn K-edge XANES spectra and (b) the corresponding  $k^3$ -weighted EXAFS spectra of pristine P2- and P3-NLMO-r. The edge position in XANES spectra is very close to that of  $\text{MnO}_2$  reference, suggesting that Mn ions in P2- and P3-NLMO-r is close to +4 valence state. Since tetravalent is the maximum valence of octahedral Mn, the redox center in P2- and P3-NLMO-r during the initial charging can thus be attributable to pure O anions.

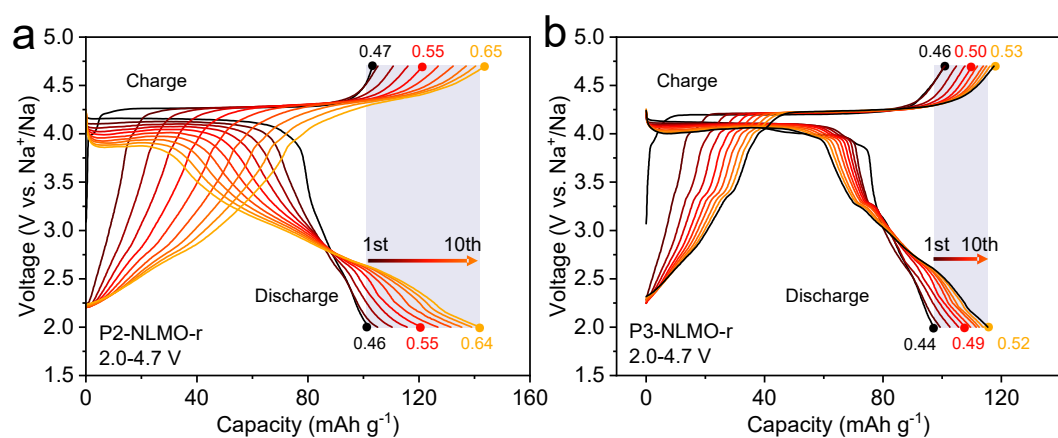


**Figure S5.** Capacity–voltage curves during the initial 10 cycles of (a) P2-NLMO-r and (b) P3-NLMO-r in the voltage range of 2.0–4.7 V at 40 mA g<sup>-1</sup>.

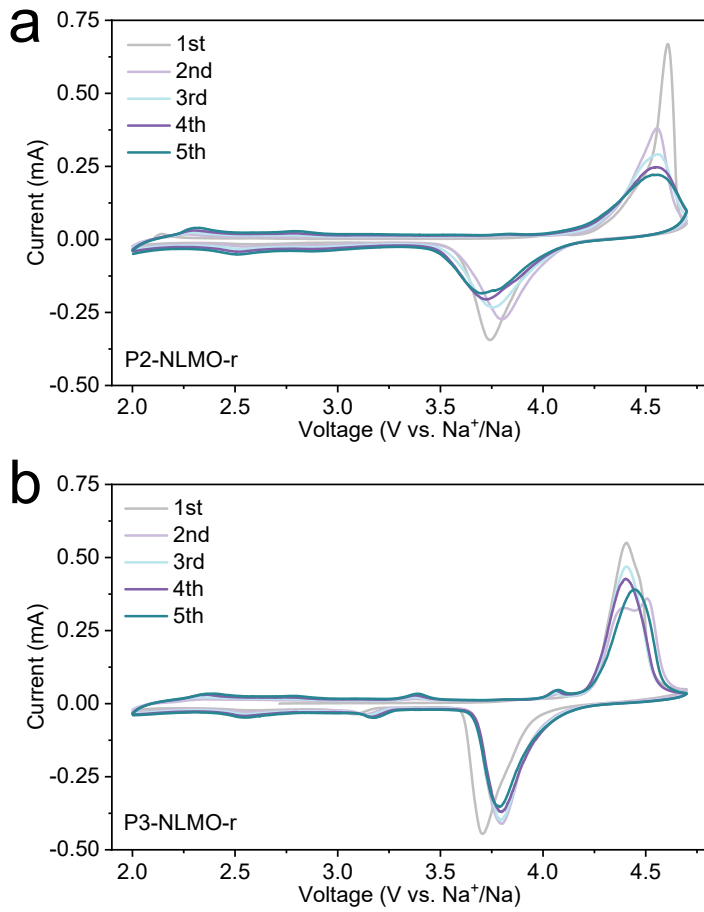


**Figure S6.** Cyclic voltammetry (CV) curves of (a) P2-NLMO-r and (b) P3-NLMO-r in the voltage range of 2.0–4.7 V at a scan rate of  $0.1 \text{ mV s}^{-1}$ .

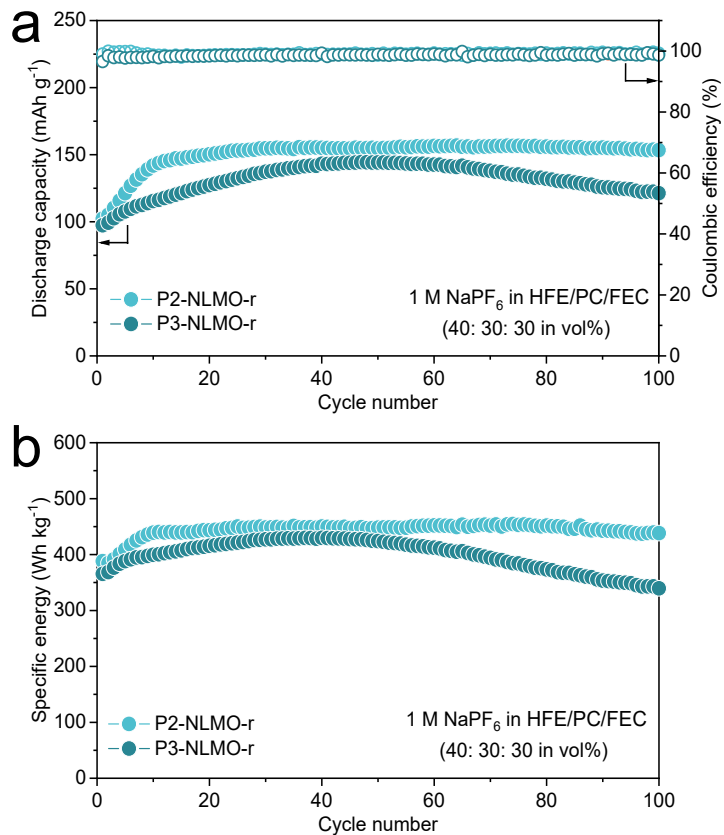


**Figure S7.** (a) Cycling stability and (b) the corresponding specific discharge energy of P2- and P3-NLMO-r in the voltage range of 2.0–4.7 V at 40 mA g<sup>-1</sup> by using 1M NaPF<sub>6</sub> in HFE/PC/FEC (40: 30: 30 in vol%) as the electrolyte. The long activation processes (~20 cycles for P2-NLMO-r and ~40 cycles for P3-NLMO-r) can be rationally attributed to the gradual activation of Mn-redox following the oxygen-centred structural rearrangements over cycling, as discussed in-detail in the main article.

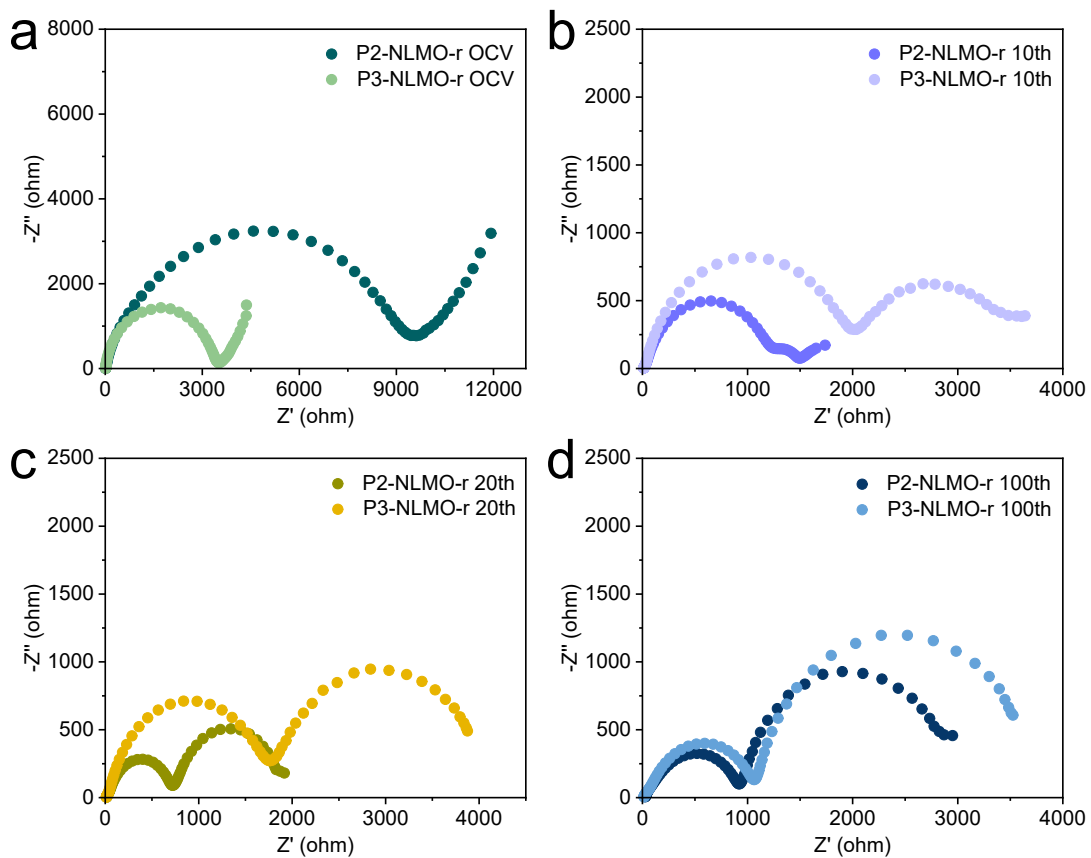


**Figure S8.** (a-d) Electrochemical impedance spectroscopy (EIS) spectra of P2- and P3-NLMO-r after different number of cycles. The  $\text{Na}^+$  diffusion kinetics in P2-NLMO-r are better than those of P3-NLMO-r after 10, 20, and 100 cycles, although it is worse than that of P3-NLMO-r at the open-circuit voltage (OCV).

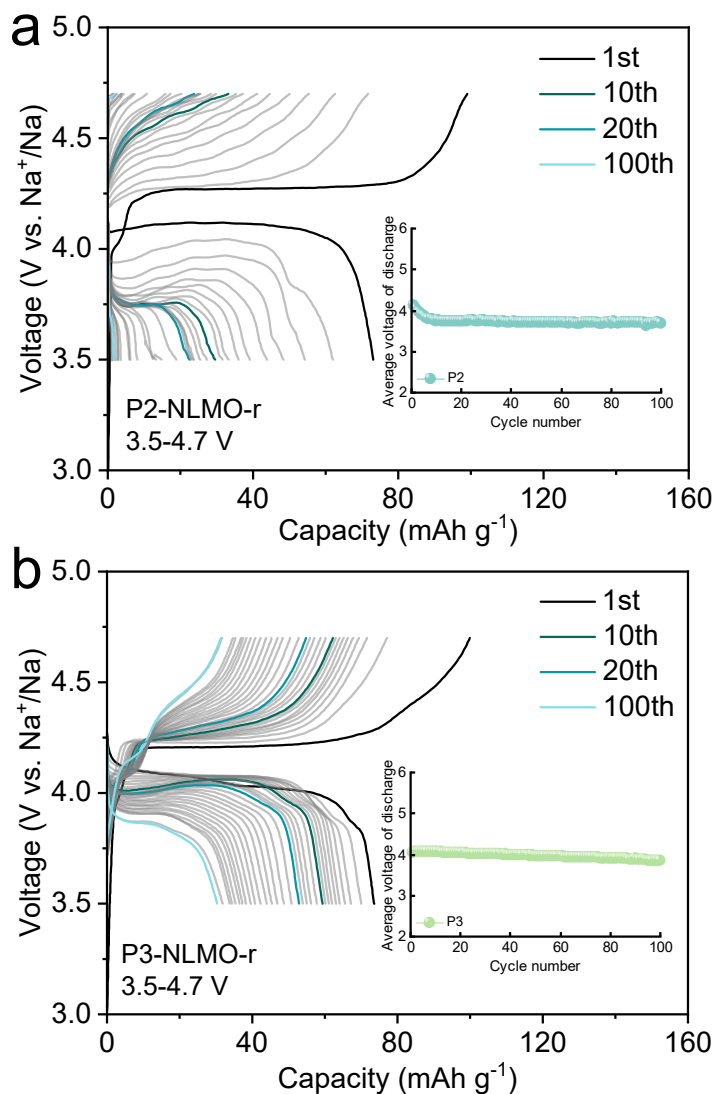


**Figure S9.** Capacity–voltage curves of (a) P2-NLMO-r and (b) P3-NLMO-r in the voltage range of 3.5–4.7 V at  $40 \text{ mA g}^{-1}$  in a Na half-cell. Inset shows the average voltage of discharge (AVoD) over cycles.

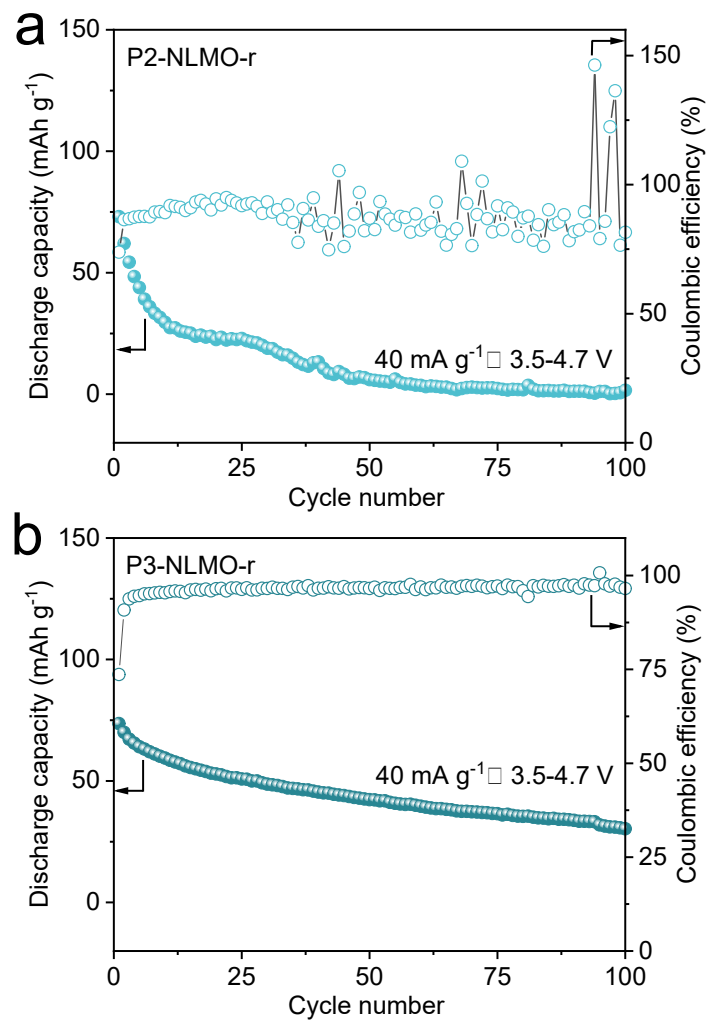


**Figure S10.** Cycling stability of (a) P2-NLMO-r and (b) P3-NLMO-r in the voltage range of 3.5–4.7 V at  $40 \text{ mA g}^{-1}$  in a Na half-cell.

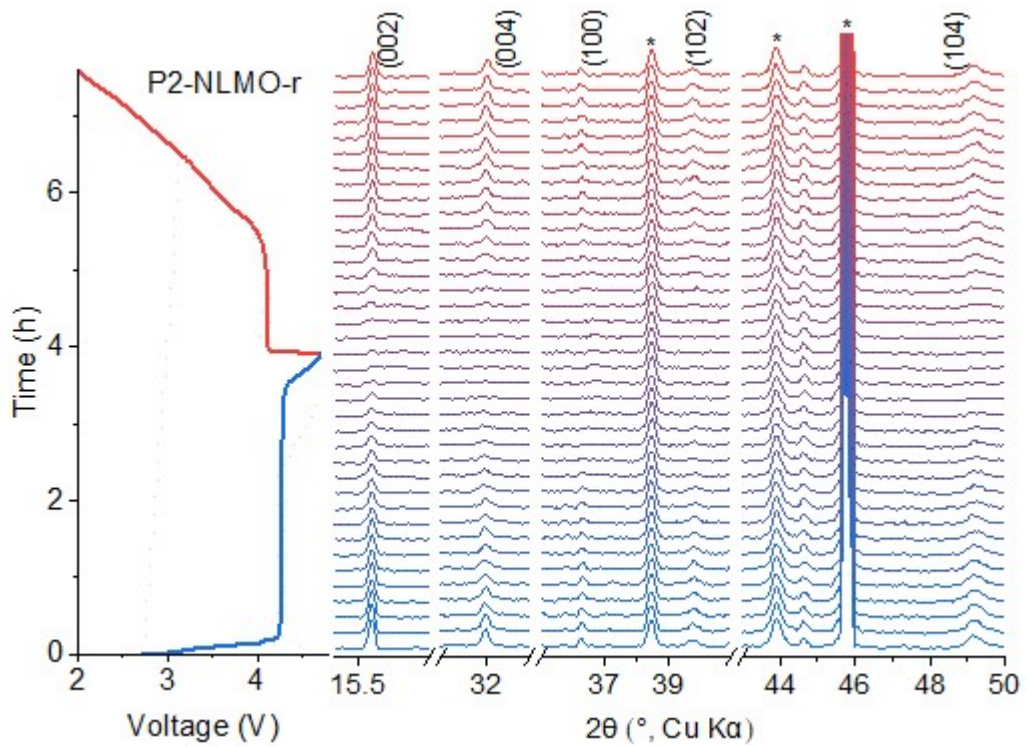


**Figure S11.** Operando XRD patterns during the first cycle of the P2-NLMO-r||Na cell cycled between 2.0-4.7 V, the left panel displays the corresponding charge/discharge voltage curves. The asterisks signify the diffraction peaks from Al foil or Be window.

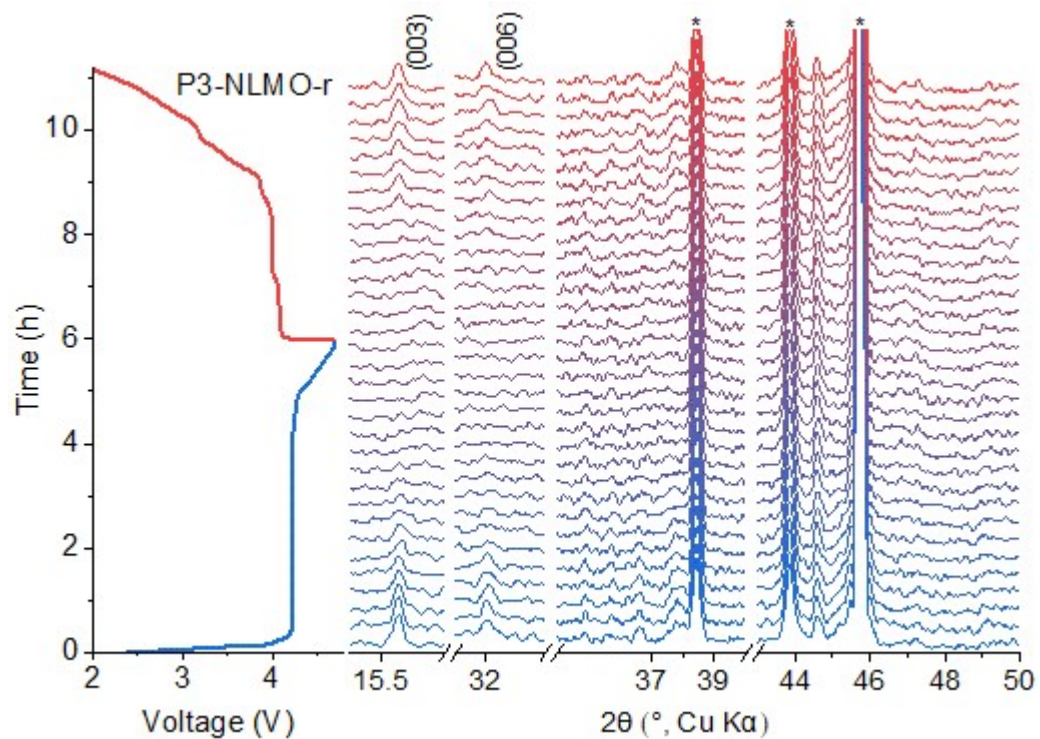


**Figure S12.** Operando XRD patterns during the first cycle of the P3-NLMO-r||Na cell cycled between 2.0-4.7 V, the left panel displays the corresponding charge/discharge voltage curves. The asterisks signify the diffraction peaks from Al foil or Be window.

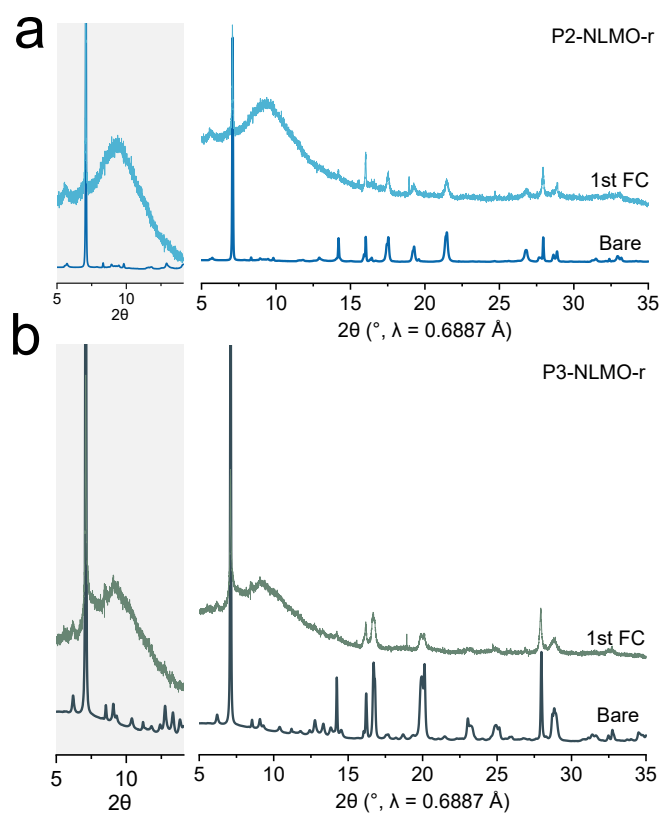


**Figure S13.** High-energy XRD patterns of (a) P2-NLMO-r and (b) P3-NLMO-r at the full-charged (FC) state after different number of cycles. The hump centered at  $\sim 9.4^\circ$  represents the signal from the capillary tube.

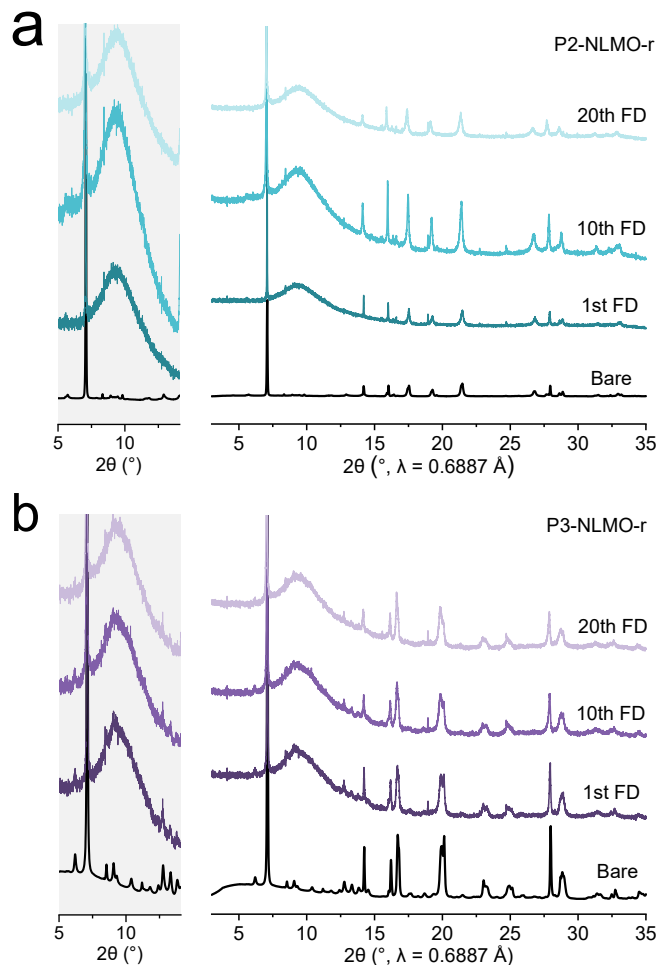


**Figure S14.** High-energy XRD patterns of (a) P2-NLMO-r and (b) P3-NLMO-r at the full-discharged (FD) state after different number of cycles. The hump centered at  $\sim 9.4^\circ$  represents the signal from the capillary tube. The preservation of all main diffraction peaks relative to the pristine electrode demonstrates the maintenance of long-range crystal structure for both P2- and P3-NLMO-r. Hence, the evolution of charge/discharge curves shown in **Figure 1e,f** is not originated from the change on crystal structure. The patterns within the  $2\theta$  range of  $5^\circ$ - $14^\circ$  (range for ribbon superstructure) were extracted and displayed in **Figure 4c,d**.

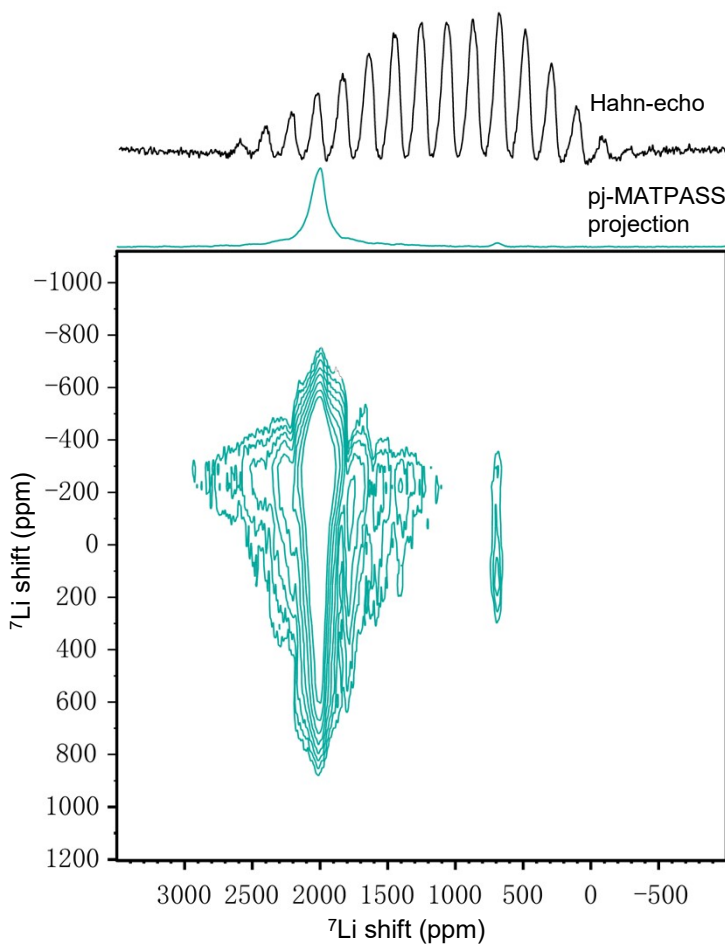


**Figure S15.** Two-dimensional  ${}^7\text{Li}$  pj-MATPASS NMR spectrum for pristine P3-NLMO-r under a moderate magnetic field of 9.4 T. The isotropic  ${}^7\text{Li}$  and  ${}^{23}\text{Na}$  resonances of P2 and P3-NLMO-r are difficult to obtain using the traditional Hahn-echo pulse sequence owing to the substantial spinning sidebands resulted from large anisotropic hyperfine interaction, as shown in the top panel. The pj-MATPASS is a pseudo two-dimensional (2D) NMR experiment with delays between pulses in the pulse sequence set according to the PASS equations, such that a sideband can be isolated in each slice of the spectrum. The intensity transferred from the isotropic resonance to each sideband can subsequently be restored to the isotropic resonance by ‘shearing’ the 2D array of data and summing the intensities of all rows.<sup>15</sup>

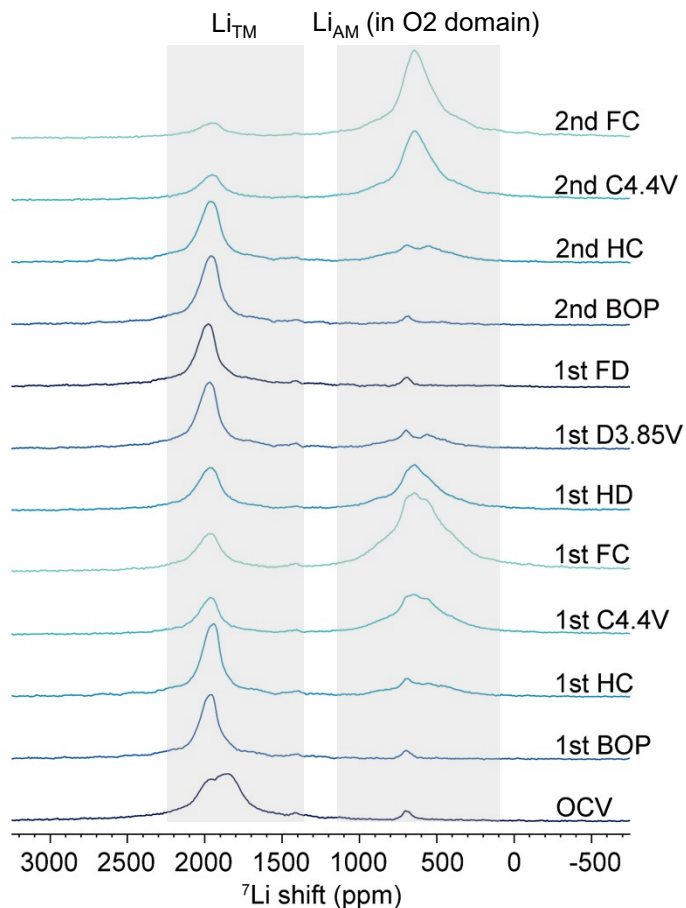


**Figure S16.** Isotropic slices of <sup>7</sup>Li pj-MATPASS NMR spectra under different charge/discharge states of P2-NLMO-r during the first charge/discharge and second charge processes. The probe temperature is controlled at 323 K and the MAS frequency is 30 kHz. The recycle interval is 10 ms and the number of scans is 20000. OCV = open circuit voltage, BOP = begin of plateau, HC = half-charged, FC = full-charged, HD = half-discharged, FD = full-discharged.

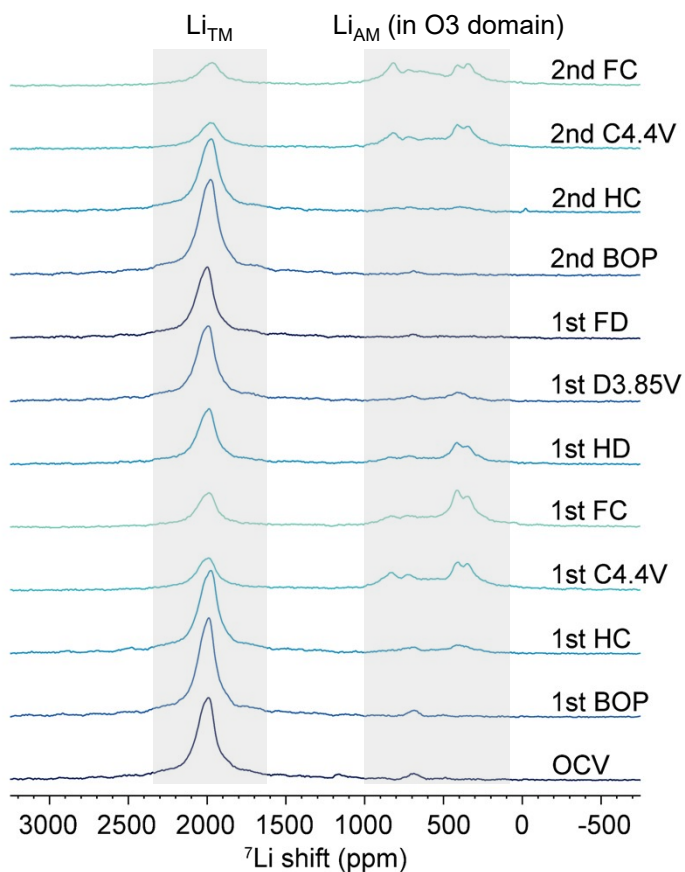


**Figure S17.** Isotropic slices of <sup>7</sup>Li pj-MATPASS NMR spectra under different charge/discharge states of P3-NLMO-r during the first charge/discharge and second charge processes. The probe temperature is controlled at 323 K and the MAS frequency is 30 kHz. The recycle interval is 10 ms and the number of scans is 20000. OCV = open circuit voltage, BOP = begin of plateau, HC = half-charged, FC = full-charged, HD = half-discharged, FD = full-discharged.

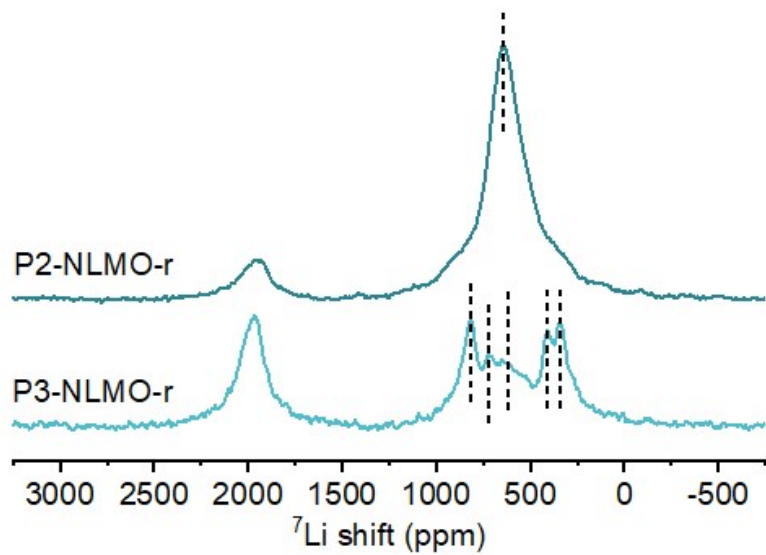


**Figure S18.** A direct comparison for the isotropic slices of <sup>7</sup>Li pj-MATPASS NMR spectra of full-charged (FC) P2- and P3-NLMO-r during the second cycle. At least five Li<sub>AM</sub> environments are observed for P3-NLMO-r, while only one can be observed for P2-NLMO-r.

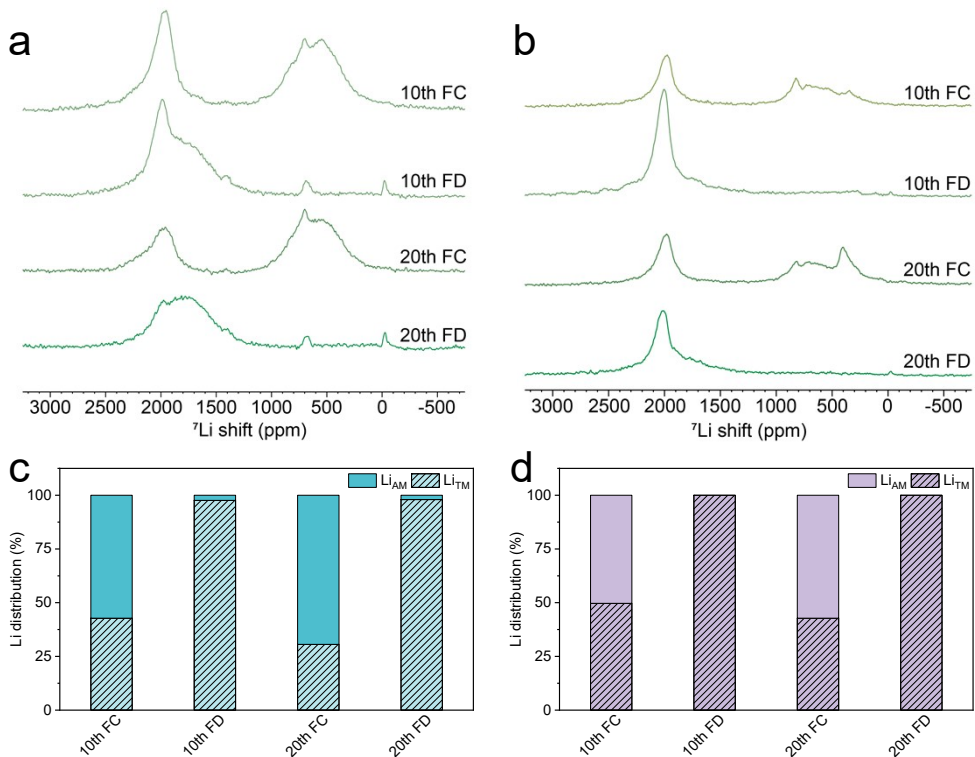


**Figure S19.** Isotropic slices of  ${}^7\text{Li}$  pj-MATPASS NMR spectra of (a) P2-NLMO-r and (b) P3-NLMO-r at the full-charged (FC) and full-discharged (FD) state of the 10th and 20th cycling. The probe temperature is controlled at 323 K and the MAS frequency is 30 kHz. The recycle interval is 10 ms and the number of scans is 20000. (c, d) The corresponding Li distribution between Li sites in the TM layer ( $\text{Li}_{\text{TM}}$ ) and Li sites in the AM layer ( $\text{Li}_{\text{AM}}$ ) for P2- and P3-NLMO-r, respectively.

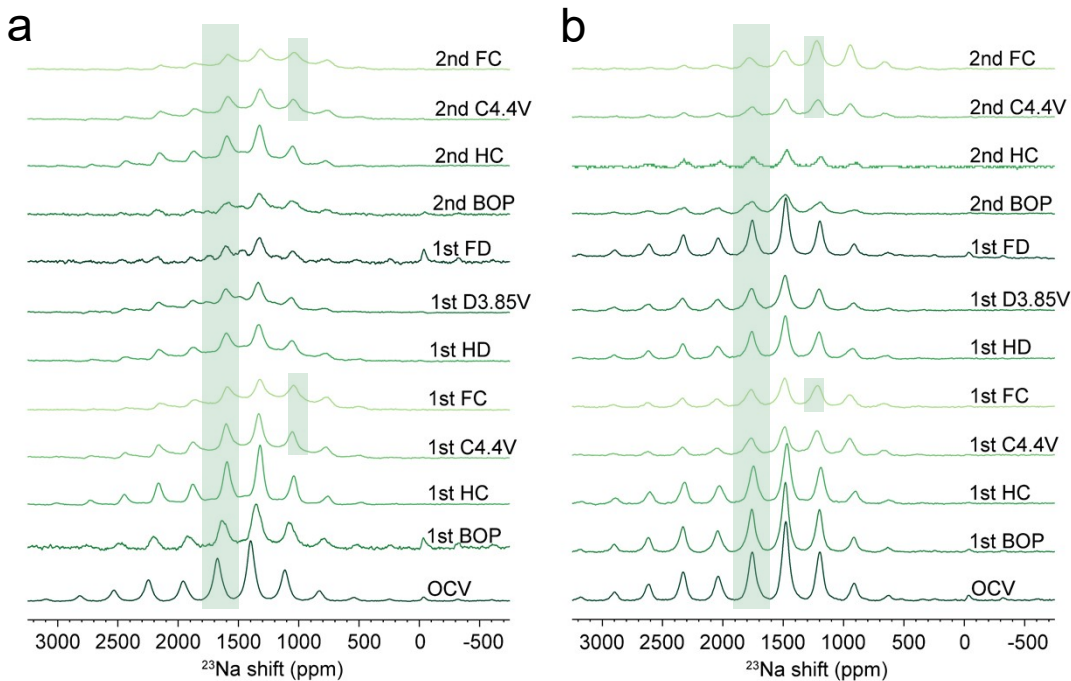


**Figure S20.** Hahn-echo  $^{23}\text{Na}$  MAS NMR spectra under different charge/discharge states of (a) P2-NLMO-r and (b) P3-NLMO-r during the first charge/discharge and second charge processes. The probe temperature is controlled at 323 K and the MAS frequency is 30 kHz, the recycle interval is 20 ms. The number of scans is 200000 for the P2-NLMO-r series and 100000 for the P3-NLMO-r series. OCV = open circuit voltage, BOP = begin of plateau, HC = half-charged, FC = full-charged, HD = half-discharged, FD = full-discharged.

The shaded areas indicate the region of isotropic  $^{23}\text{Na}$  resonances as confirmed via pj-MATPASS NMR results (**Figure 2c, d**) while the rest of peaks are from spinning sidebands (SSBs). It can be seen that the formation of new  $^{23}\text{Na}$  signals representing Na in O<sub>2</sub>-type domain in P2-NLMO-r series and Na in O<sub>3</sub>-type domain in P3-NLMO-r series is hardly seen by the one-dimensional Hahn-echo pulse sequence, highlighting the importance of using pj-MATPASS technique in this study.

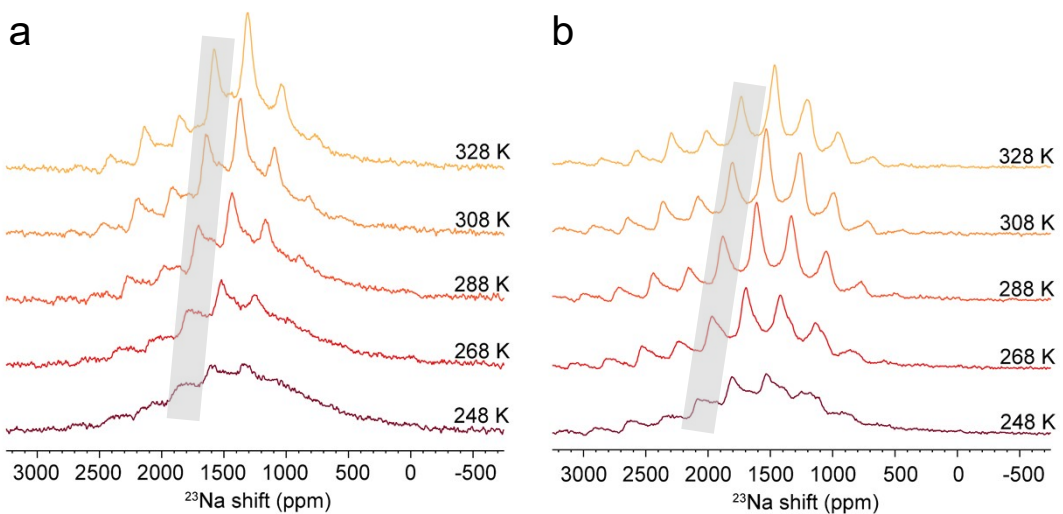


**Figure S21.** Variable-temperature Hahn-echo  $^{23}\text{Na}$  MAS NMR spectra for (a) P2-NLMO-r and (b) P3-NLMO-r at full-charged (FC) state. The number of scans is 200000 for the P2-NLMO-r series and 100000 for the P3-NLMO-r series. As the peaks signifying  $\text{Na}^+$  in O<sub>2</sub>/O<sub>3</sub>-type domains are overlapped with spinning sidebands, we only focus on the evolution of “Na in P2/P3-type domain” peaks under variable-temperature, as marked by shaded areas.

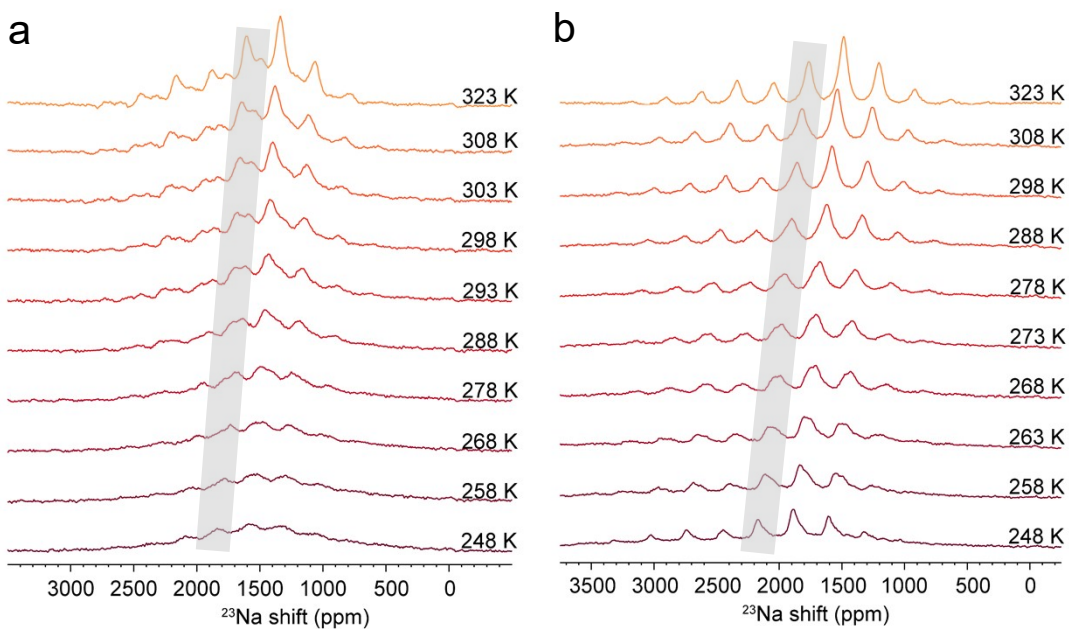


**Figure S22.** Variable-temperature Hahn-echo  $^{23}\text{Na}$  MAS NMR spectra for (a) P2-NLMO-r and (b) P3-NLMO-r at 3.85 V-discharged state. The number of scans is 200000 for the P2-NLMO-r series and 100000 for the P3-NLMO-r series. The isotropic  $^{23}\text{Na}$  signals representing Na in P2/P3-type domains are marked by shaded areas.

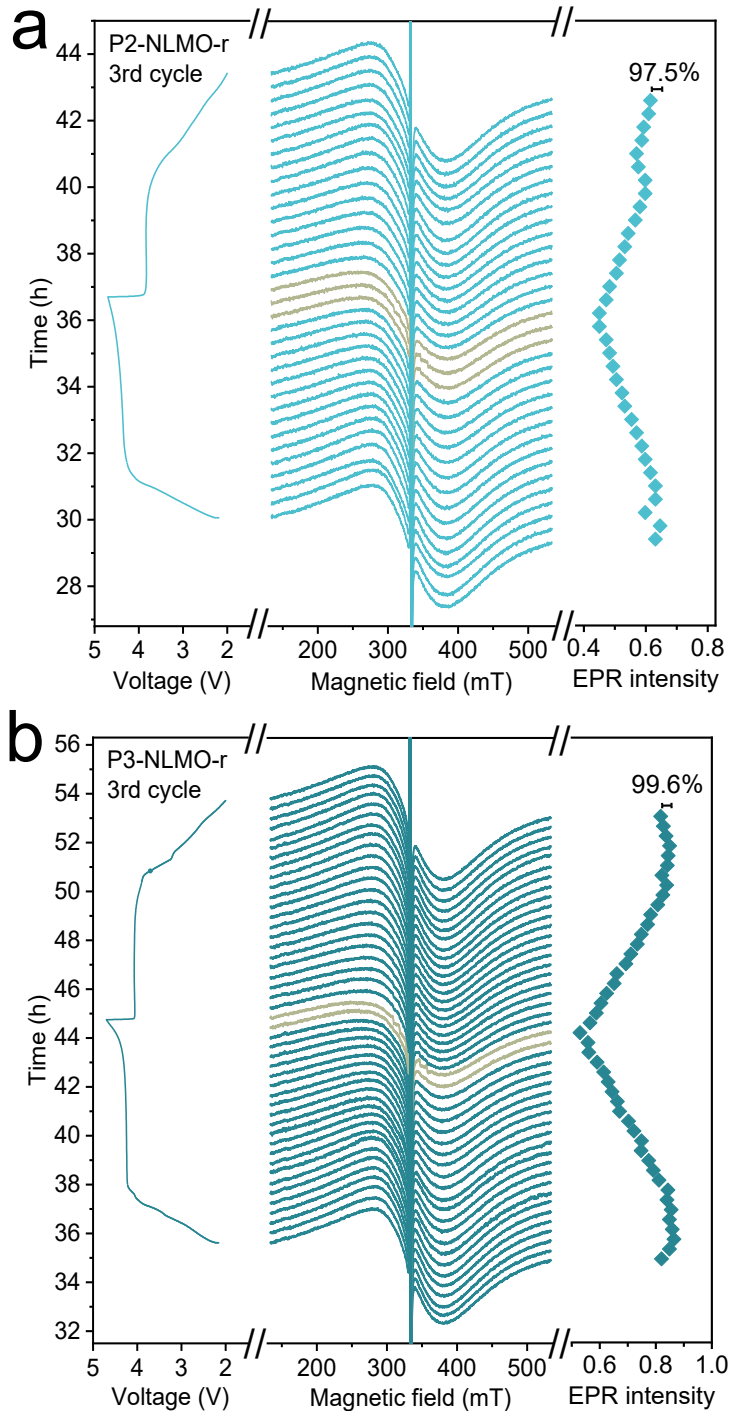


**Figure S23.** Operando EPR spectra during the third cycle of the (a) P2-NLMO-r||Na and (b) P3-NLMO-r||Na cell cycled between 2.0-4.7 V. The corresponding voltage *versus* time curves are shown on the left panel, the EPR intensities (peak-to-trough values) are shown on the right panel.

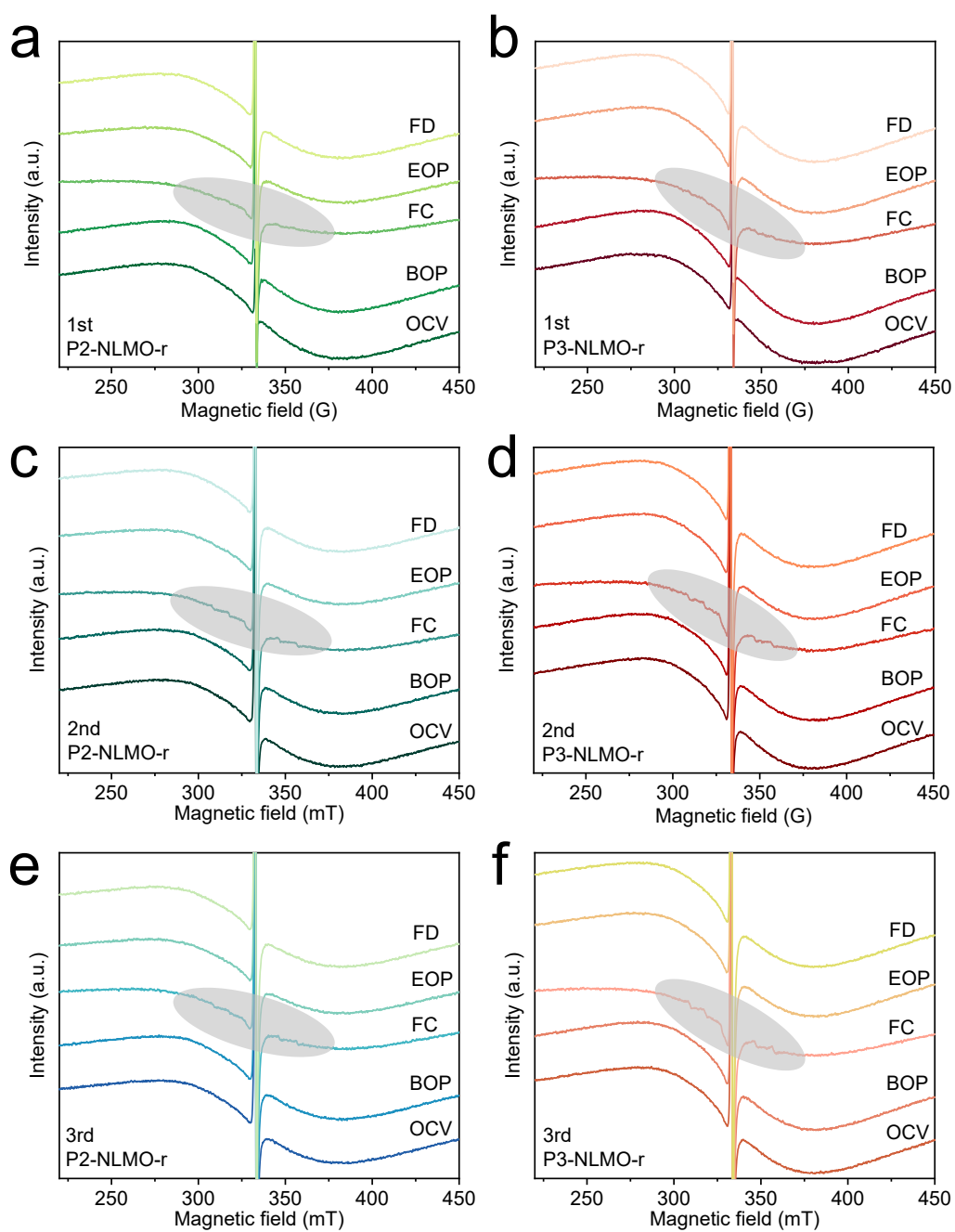


**Figure S24.** Representative EPR spectra extracted from the operando EPR results of P2- and P3-NLMO-r: (a, b) initial cycle, (c, d) second cycle, (e, f) third cycle. OCV = open circuit voltage, BOP = begin of plateau upon charging, FC = full-charged, EOP = end of plateau upon discharging, FD = full-discharged.

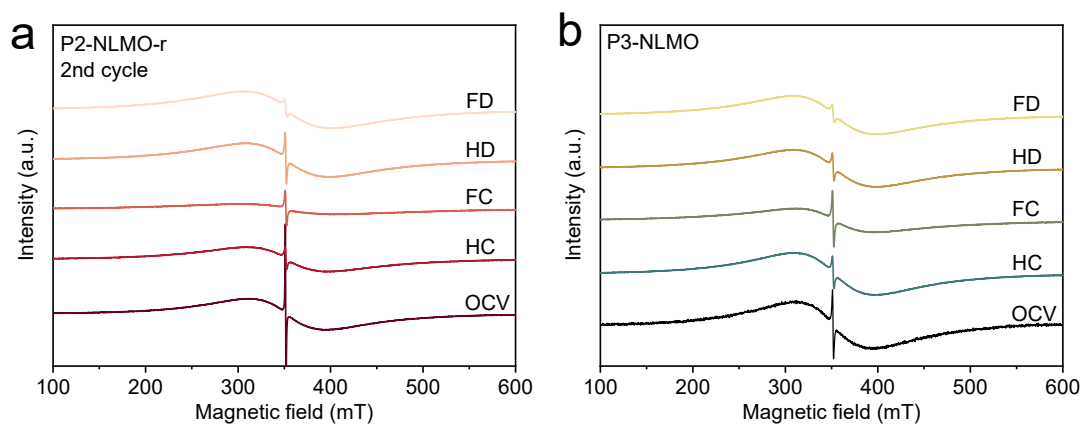


**Figure S25.** Ex situ EPR spectra of (a) P2-NLMO-r and (b) P3-NLMO-r during the second cycle. OCV = open circuit voltage, HC = half-charged, FC = full-charged, HD = half-discharged, FD = full-discharged.

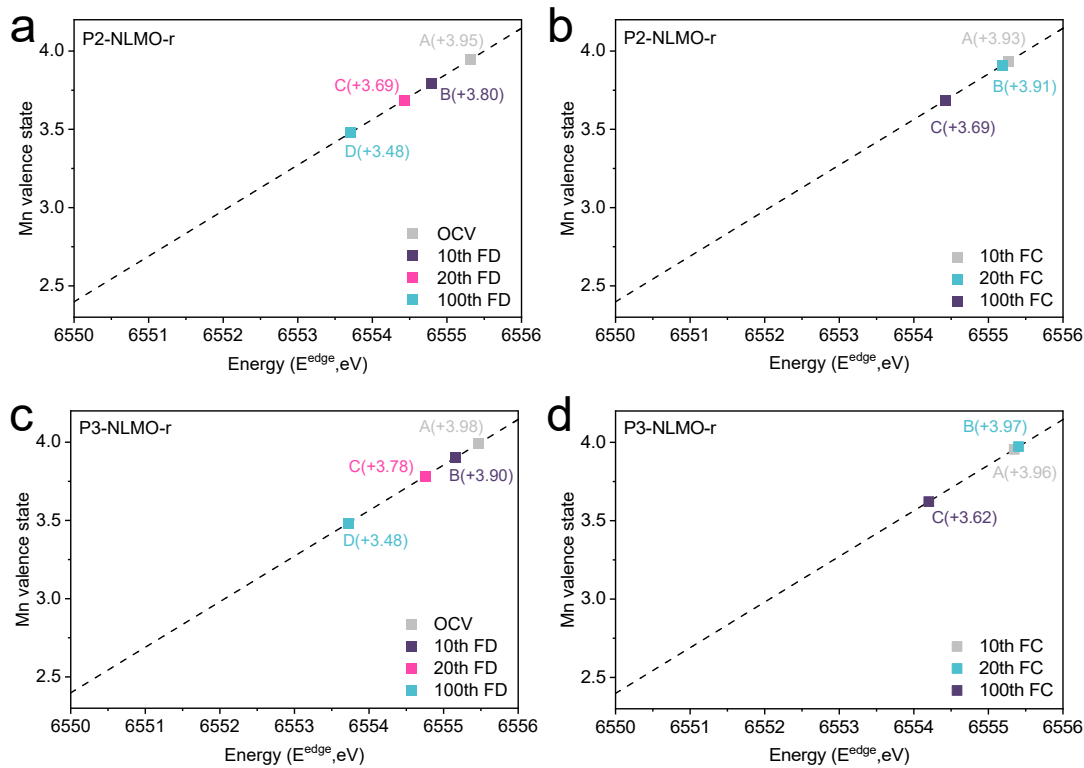


**Figure S26.** Evolution of the estimated valence state of Mn for (a, b) P2-NLMO-r and (c, d) P3-NLMO-r over cycling under full-charged (FC) and full-discharged (FD) states.

The linear calibration between Mn valence states and the K-edge positions was determined by the integral method<sup>16, 17</sup> using  $\text{Mn}_3\text{O}_4$ ,  $\text{Mn}_2\text{O}_3$  and  $\text{MnO}_2$  as reference samples. Integration was carried out between  $\mu_1 = 0.15$  and  $\mu_2 = 1.0$  on each normalized spectrum to remove contributions from the pre-edge and account for variations in the shape of the absorption edge on the average edge energy. The  $E^{\text{edge}}$  was calculated using the following formula:

$$E^{\text{edge}} = E_1 + \frac{[\mu_2(E_2 - E_1) - \text{Area}]}{\mu_2 - \mu_1}$$

where *Area* is the integral area between  $(\mu_2, E_2)$  and  $(\mu_1, E_1)$

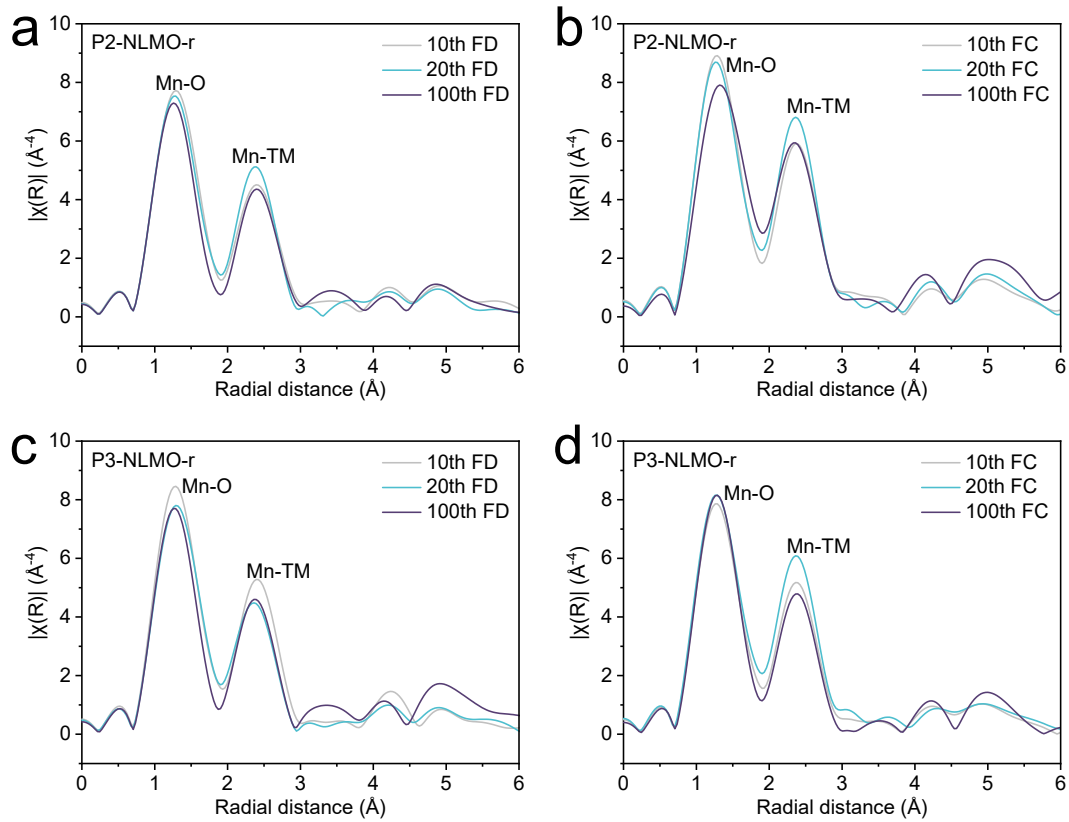


**Figure S27.** The  $k^3$ -weighted Mn K-edge EXAFS spectra of (a, b) P2-NLMO-r and (c, d) P3-NLMO-r over cycling under full-discharged (FD) and full-charged (FC) states.

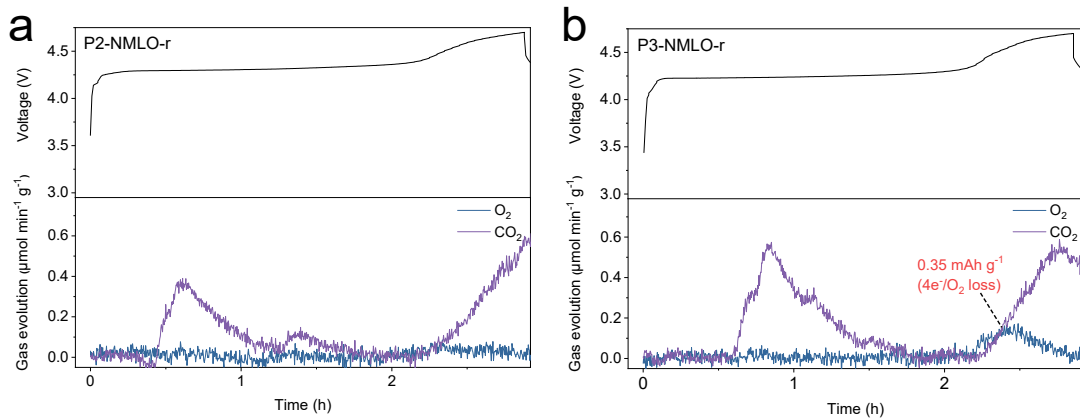


**Figure S28.** OEMS results of  $O_2/CO_2$  evolution during the first charge process of (a) P2-NLMO-r and (b) P3-NLMO-r. The electrolyte used was 1 M  $NaPF_6$  in HFE/PC/FEC (4: 3: 3 in volume) and the charging rate was 40 mA  $g^{-1}$ . The amount of evolution of the  $O_2$  ( $\mu\text{mol}$ ) is converted to the specific capacity ( $\text{mAh g}^{-1}$ ) based on previous literature.<sup>18</sup>

Although P3-NLMO-r shows more apparent  $O_2$  loss during the initial charging as compared to P2-NLMO-r, the specific capacity of the OAR measured by OEMS is only 0.35  $\text{mAh g}^{-1}$  for P3-NLMO-r. Such value is significantly lower than its initial charge capacity (102.4  $\text{mAh g}^{-1}$ ). Hence, we conclude that the evolution of the  $O_2$  gas is negligible for both P2-NLMO-r and P3-NLMO-r, making them very suitable benchmark systems to investigating the influence of superstructure evolution on the stability of OAR upon cycling.

**Table S1.** Rietveld refinement results on the high-energy XRD ( $\lambda = 0.6887 \text{ \AA}$ ) patterns

of the as-prepared P2-NLMO-r.

<sup>a</sup>Space group P1. <sup>b</sup> $a = 9.922 \text{ \AA}$ ,  $b = 7.537 \text{ \AA}$ ,  $c = 11.5230 \text{ \AA}$ ,  $\alpha = 76.188^\circ$ ,  $\beta = 89.69^\circ$ ,  
 $\gamma = 108.74^\circ$ ,  $V = 789.297 \text{ \AA}^3$ . <sup>c</sup> $R_{\text{Bragg}} = 8.00\%$ ,  $\chi^2 = 2.48$

Atom	x	y	z	Occ.
Na1	-1.01883	-0.08329	0.99946	1.000
Na2	1.46122	-0.07423	1.25958	1.000
Na3	1.08259	1.03114	0.09222	1.000
Na4	1.04806	0.53588	0.24373	1.000
Na5	1.20045	0.73420	0.24512	1.000
Na6	0.23573	0.95343	0.59445	1.000
Na7	0.76439	0.18309	0.19933	1.000
Na8	0.31332	0.33518	0.29401	1.000
Na9	-0.60043	0.92270	0.05661	1.000
Na10	0.56683	0.97440	0.01706	1.000
Na11	-0.06800	0.09475	0.27751	1.000
Na12	0.58162	0.57196	0.26238	1.000
Mn1	0.36158	0.55949	0.04407	1.000
Mn2	0.95458	0.66696	0.00341	1.000
Mn3	0.95039	0.80600	0.50321	1.000
Mn4	0.45039	0.80600	0.50321	1.000
Mn5	0.34614	0.39473	0.49930	1.000
Mn6	0.84614	0.39473	0.49930	1.000
Mn7	0.10894	0.40432	-0.00540	1.000
Mn8	0.57777	0.38082	0.01348	1.000
Mn9	0.27794	0.17551	0.00588	1.000
Mn10	0.81906	0.20741	0.00823	1.000
Mn11	0.19995	0.80623	0.00327	1.000
Mn12	0.69995	0.80623	0.00327	1.000
Mn13	0.15150	0.60760	0.50093	1.000
Mn14	0.65150	0.60760	0.50093	1.000
Mn15	0.04749	0.19671	0.49674	1.000
Mn16	0.54550	0.17086	0.51559	1.000
O1	0.13061	0.17561	0.09057	1.000
O2	0.63061	0.17561	0.09057	1.000
O3	0.02267	0.74633	0.09552(	1.000
O4	0.52267	0.74633	0.09552	1.000
O5	0.27387	0.43872	0.90883	1.000
O6	0.77387	0.43872	0.90883	1.000

O7	0.30847	0.96652	0.09614	1.000
O8	0.80847	0.96652	0.09614	1.000
O9	0.22387	0.56477	0.09093	1.000
O10	0.72387	0.56477	0.09093	1.000
O11	0.18917	0.03698	0.90399	1.000
O12	0.68917	0.03698	0.90399	1.000
O13	0.07355	0.64128	0.90901	1.000
O14	0.57355	0.64128	0.90901	1.000
O15	0.42451	0.36238	0.09066	1.000
O16	0.92451	0.36238	0.09066	1.000
O17	0.47507	0.25697	0.90449	1.000
O18	0.97507	0.25697	0.90449	1.000
O19	0.36692	0.82773	0.90934	1.000
O20	0.86692	0.82773	0.90934	1.000
O21	0.20366	0.17510	0.59087	1.000
O22	0.70366	0.17510	0.59087	1.000
O23	0.07651	0.03741	0.40360	1.000
O24	0.57651	0.03741	0.40360	1.000
O25	0.99429	0.64088	0.40931	1.000
O26	0.49429	0.64088	0.40931	1.000
O27	0.09817	0.74642	0.59546	1.000
O28	0.59817	0.74642	0.59546	1.000
O29	0.00308	0.36175	0.59079	1.000
O30	0.50308	0.36175	0.59079	1.000
O31	0.29393	0.82717	0.40936	1.000
O32	0.79393	0.82717	0.40936	1.000
O33	0.19180	0.43797	0.40936	1.000
O34	0.69180	0.43797	0.40936	1.000
O35	0.42170	0.96594	0.59605	1.000
O36	0.92170	0.96594	0.59605	1.000
O37	0.30577	0.56452	0.59130	1.000
O38	0.80577	0.56452	0.59130	1.000
O39	0.39985	0.25612	0.40445	1.000
O40	0.89985	0.25612	0.40445	1.000
Li1	-0.00120	0.00165	0.00005	1.000
Li2	0.49880	0.00165	0.00005	1.000
Li3	0.24886	0.00131	0.49999	1.000
Li4	0.74886	0.00131	0.49999	1.000

**Table S2.** Rietveld refinement results on the high-energy XRD ( $\lambda = 0.6887 \text{ \AA}$ ) patterns

of the as-prepared P3-NLMO-r.

<sup>a</sup>Space group P1. <sup>b</sup> $a = 9.866 \text{ \AA}$ ,  $b = 7.539 \text{ \AA}$ ,  $c = 16.892 \text{ \AA}$ ,  $\alpha = 82.56^\circ$ ,  $\beta = 82.38^\circ$ ,  $\gamma = 70.94^\circ$ ,  $V = 1172.112 \text{ \AA}^3$ . <sup>c</sup> $R_{\text{Bragg}} = 8.53\%$ ,  $\chi^2 = 6.90$

Atom	x	y	z	Occ.
Na1	2.41483	-0.85397	0	1.000
Na2	-0.49383	1.08527	-0.94252	1.000
Na3	1.00082	0.55274	0.66691	1.000
Na4	-0.53376	2.31967	3.13664	1.000
Na5	0.11646	0.40901	0.83629	1.000
Na6	0.71526	0.25729	0.83102	1.000
Na7	0.87287	0.68784	0.50660	1.000
Na8	0.34299	0.69243	0.50489	1.000
Na9	0.62503	0.31325	0.49403	1.000
Na10	0.15490	0.30502	0.49446	1.000
Na11	0.95072	0.07660	0.50161	1.000
Na12	0.54869	0.91981	0.49820	1.000
Na13	0.74988	0.12982	0.16571	1.000
Na14	0.41282	0.68498	0.69329	1.000
Na15	0.24065	1.74169	0.69653	1.000
Na16	-0.03008	1.03657	-0.17526	1.000
Na17	0.31063	1.13261	0.15119	1.000
Na18	0.70597	0.51809	0.21494	1.000
Mn1	0.30031	0.80263	0.01322	1.000
Mn2	0.79824	0.80767	-0.00279	1.000
Mn3	0.20127	0.19124	0.00291	1.000
Mn4	0.70076	0.19428	0.00236	1.000
Mn5	0.40266	0.39190	0.00046	1.000
Mn6	0.90096	0.39312	0.00111	1.000
Mn7	0.23502	0.05950	0.66781	1.000
Mn8	0.73332	0.06120	0.66773	1.000
Mn9	0.13094	0.47260	0.66471	1.000
Mn10	0.63070	0.47543	0.66447	1.000
Mn11	0.03368	0.85927	0.66958	1.000
Mn12	0.53299	0.86201	0.66989	1.000
Mn13	0.96496	0.13971	0.32838	1.000
Mn14	0.46385	0.13981	0.33256	1.000
Mn15	0.06805	0.72584	0.33386	1.000
Mn16	0.56806	0.72631	0.33314	1.000

Mn17	0.09868	0.60556	-0.00104	1.000
Mn18	0.59702	0.60718	-0.00110	1.000
Mn19	0.36759	0.52689	0.33303	1.000
Mn20	0.86676	0.52596	0.33717	1.000
Mn21	0.93069	0.27370	0.66622	1.000
Mn22	0.42898	0.27507	0.66667	1.000
Mn23	0.26385	0.93989	0.33249	1.000
Mn24	0.76354	0.94024	0.33187	1.000
O1	0.04539	0.22214	0.93974	1.000
O2	0.54709	0.22312	0.93769	1.000
O3	0.16832	0.98111	0.06555	1.000
O4	0.66991	0.98533	0.06346	1.000
O5	0.32930	0.01425	0.93636	1.000
O6	0.83148	0.01771	0.93439	1.000
O7	0.45264	0.77587	0.06154	1.000
O8	0.95420	0.77619	0.06052	1.000
O9	0.05231	0.39032	0.06397	1.000
O10	0.55344	0.38844	0.06140	1.000
O11	0.24724	0.40889	0.93888	1.000
O12	0.74847	0.41099	0.93757	1.000
O13	0.34775	0.19976	0.06467	1.000
O14	0.84387	0.20500	0.06586	1.000
O15	0.15587	0.79349	0.93393	1.000
O16	0.65206	0.79956	0.93527	1.000
O17	0.25185	0.58781	0.06184	1.000
O18	0.75198	0.58990	0.06100	1.000
O19	0.44620	0.61105	0.93765	1.000
O20	0.94720	0.60846	0.93633	1.000
O21	0.07928	0.07732	0.60594	1.000
O22	0.57938	0.07913	0.60512	1.000
O23	0.88455	0.05840	0.73067	1.000
O24	0.38534	0.05638	0.72934	1.000
O25	0.18066	0.86639	0.73121	1.000
O26	0.67677	0.87268	0.73246	1.000
O27	0.98753	0.46215	0.60164	1.000
O28	0.48393	0.46753	0.60274	1.000
O29	0.27847	0.27878	0.60535	1.000
O30	0.77925	0.27733	0.60330	1.000
O31	0.08376	0.25550	0.72951	1.000
O32	0.58454	0.25757	0.72838	1.000
O33	0.87842	0.89059	0.60594	1.000
O34	0.37973	0.89000	0.60546	1.000
O35	0.16127	0.68161	0.60325	1.000
O36	0.66438	0.68574	0.60208	1.000

O37	0.00058	0.64948	0.73260	1.000
O38	0.50330	0.65234	0.73085	1.000
O39	0.28409	0.44381	0.72938	1.000
O40	0.78606	0.44407	0.72797	1.000
O41	0.11816	0.11080	0.39335	1.000
O42	0.61998	0.10849	0.39575	1.000
O43	0.11368	0.94272	0.26857	1.000
O44	0.61157	0.94464	0.27181	1.000
O45	0.41736	0.92024	0.39531	1.000
O46	0.91894	0.92371	0.39370	1.000
O47	0.41482	0.74561	0.27012	1.000
O48	0.91349	0.74215	0.27170	1.000
O49	-0.00443	0.35174	0.26745	1.000
O50	0.49721	0.34582	0.26918	1.000
O51	0.01368	0.53389	0.39822	1.000
O52	0.51085	0.53713	0.39701	1.000
O53	0.32084	0.12921	0.26870	1.000
O54	0.81712	0.13250	0.26762	1.000
O55	0.33389	0.32144	0.39635	1.000
O56	0.83550	0.31341	0.39778	1.000
O57	0.21091	0.55780	0.27001	1.000
O58	0.71398	0.55594	0.27212	1.000
O59	0.22000	0.72186	0.39380	1.000
O60	0.71867	0.72305	0.39712	1.000
Li1	0.49983	-0.00054	0.00014	1.000
Li2	-0.00007	-0.00064	-0.00014	1.000
Li3	0.33210	0.66727	0.66668	1.000
Li4	0.83202	0.66737	0.66706	1.000
Li5	0.16558	0.33361	0.33303	1.000
Li6	0.66600	0.33247	0.33312	1.000

**Table S3.** ICP-OES results for the dissolved Li/Mn content after 1 and 5 cycles. These values are set relative to the content of Na<sup>+</sup> in the electrolyte. To perform the ICP-OES measurements of Li/Mn dissolution, the separators (GF/D) were immersed in 2 mL dimethyl carbonate (DMC) for one day. Subsequently, the mixtures were filtrated and the obtained DMC solutions were attenuated with deionized water and acidized with 1 M HCl.

Sample	Na	Li	Mn
P2-NLMO-r, 1st cycle	1	0.0015	0
P2-NLMO-r, 5th cycle	1	0.0038	0.0017
P3-NLMO-r, 1st cycle	1	0.0015	0
P3-NLMO-r, 5th cycle	1	0.0045	0.0018

## Supplementary references

1. H. Ren, Y. Li, Q. Li, K. Zhang, Y. Zhao, C. Wu and Y. Bai, *Energy Storage Mater.*, 2023, **57**, 59-68.
2. A. Gao, Q. Zhang, X. Li, T. Shang, Z. Tang, X. Lu, Y. Luo, J. Ding, W. H. Kan, H. Chen, W. Yin, X. Wang, D. Xiao, D. Su, H. Li, X. Rong, X. Yu, Q. Yu, F. Meng, C. Nan, C. Delmas, L. Chen, Y.-S. Hu and L. Gu, *Nat. Sustain.*, 2021, **5**, 214-224.
3. J. W. Somerville, A. Sobkowiak, N. Tapia-Ruiz, J. Billaud, J. G. Lozano, R. A. House, L. C. Gallington, T. Ericsson, L. Häggström, M. R. Roberts, U. Maitra and P. G. Bruce, *Energy Environ. Sci.*, 2019, **12**, 2223-2232.
4. S. M. Kang, D. Kim, K. S. Lee, M. S. Kim, A. Jin, J. H. Park, C. Y. Ahn, T. Y. Jeon, Y. H. Jung, S. H. Yu, J. Mun and Y. E. Sung, *Adv. Sci.*, 2020, **7**, 2001263.
5. Q. Wang, S. Mariyappan, G. Rousse, A. V. Morozov, B. Porcheron, R. Dedryvere, J. Wu, W. Yang, L. Zhang, M. Chakir, M. Avdeev, M. Deschamps, Y. S. Yu, J. Cabana, M. L. Doublet, A. M. Abakumov and J. M. Tarascon, *Nat. Mater.*, 2021, **20**, 353-361.
6. F. Dogan, B. R. Long, J. R. Croy, K. G. Gallagher, H. Iddir, J. T. Russell, M. Balasubramanian and B. Key, *J. Am. Chem. Soc.*, 2015, **137**, 2328-2335.
7. J. Xu, D. H. Lee, R. J. Clément, X. Yu, M. Leskes, A. J. Pell, G. Pintacuda, X.-Q. Yang, C. P. Grey and Y. S. Meng, *Chem. Mater.*, 2014, **26**, 1260-1269.
8. R. A. House, U. Maitra, M. A. Perez-Osorio, J. G. Lozano, L. Jin, J. W. Somerville, L. C. Duda, A. Nag, A. Walters, K. J. Zhou, M. R. Roberts and P. G. Bruce, *Nature*, 2020, **577**, 502-508.
9. C. Zhao, C. Li, H. Liu, Q. Qiu, F. Geng, M. Shen, W. Tong, J. Li and B. Hu, *J. Am. Chem. Soc.*, 2021, **143**, 18652-18664.
10. C. Chazel, M. Ménétrier, L. Croguennec and C. Delmas, *Magn. Reson. Chem.*, 2005, **43**, 849 – 857.
11. Z. Liu, Y.-Y. Hu, M. T. Dunstan, H. Huo, X. Hao, H. Zou, G. Zhong, Y. Yang and C. P. Grey, *Chem. Mater.*, 2014, **26**, 2513-2521.
12. B. Song, M. Tang, E. Hu, O. J. Borkiewicz, K. M. Wiaderek, Y. Zhang, N. D.

- Phillip, X. Liu, Z. Shadike, C. Li, L. Song, Y.-Y. Hu, M. Chi, G. M. Veith, X.-Q. Yang, J. Liu, J. Nanda, K. Page and A. Huq, *Chem. Mater.*, 2019, **31**, 3756-3765.
13. H. Liu, C. Zhao, Q. Qiu, B. Hu, F. Geng, J. Li, W. Tong, B. Hu and C. Li, *J. Phys. Chem. Lett.*, 2021, **12**, 8740-8748.
14. C. Zhao, H. Liu, F. Geng, B. Hu and C. Li, *Energy Storage Mater.*, 2022, **48**, 290-296.
15. I. Hung, L. Zhou, F. Pourpoint, C. P. Grey and Z. Gan, *J. Am. Chem. Soc.*, 2012, **134**, 1898-1901.
16. H. Dau, P. Liebisch and M. Haumann, *Anal. Bioanal. Chem.*, 2003, **376**, 562-583.
17. X. Cao, H. Li, Y. Qiao, P. He, Y. Qian, X. Yue, M. Jia, J. Cabana and H. Zhou, *Joule*, 2022, **6**, 1290-1303.
18. Z. Wu, G. Zeng, J. Yin, C.-L. Chiang, Q. Zhang, B. Zhang, J. Chen, Y. Yan, Y. Tang, H. Zhang, S. Zhou, Q. Wang, X. Kuai, Y.-G. Lin, L. Gu, Y. Qiao and S.-G. Sun, *ACS Energy Lett.*, 2023, **8**, 4806-4817.